Experimental Evaluation of Optically Polished Aluminum Panels on the Deep Space Network's 34 Meter Antenna

V. Vilnrotter[1]

Jet Propulsion Laboratory, California Institute of Technology
4800 Oak Grove Dr.
Pasadena, CA 91109
(818) 354-2745
Victor.A.Vilnrotter@jpl.nasa.gov

Abstract: The potential development of large aperture ground-based "photon bucket" optical receivers for deep space communications has received considerable attention recently. One approach currently under investigation is to polish the aluminum reflector panels of 34-meter microwave antennas to high reflectance, and accept the relatively large spotsize generated by state-of-the-art polished aluminum panels. Theoretical analyses of receiving antenna pointing, temporal synchronization and data detection have been addressed in previous papers. Here we describe the experimental effort currently underway at the Deep Space Network (DSN) Goldstone Communications Complex in California, to test and verify these concepts in a realistic operational environment. Two polished aluminum panels (a standard DSN panel polished to high reflectance, and a custom designed aluminum panel with much better surface quality) have been mounted on the 34 meter research antenna at Deep-Space Station 13 (DSS-13), and a remotely controlled CCD camera with a large CCD sensor in a weather-proof container has been installed next to the subreflector, pointed directly at the custom polished panel. The point-spread function (PSF) generated by the Vertex polished panel has been determined to be smaller than the sensor of the CCD camera, hence a detailed picture of the PSF can be obtained every few seconds, and the sensor array data processed to determine the center of the intensity distribution. In addition to estimating the center coordinates, expected communications performance can also been evaluated with the recorded data. The results of preliminary pointing experiments with the Vertex polished panel receiver using the planet Jupiter to simulate the PSF generated by a deep-space optical transmitter are presented and discussed in this paper.

I. Introduction

The option to provide an optical communications capability for the 34-meter microwave antennas of the Deep-Space Network (DSN) has received considerable attention recently. This concept is predicated on the assumption that the existing RF capabilities of these microwave antennas would not be compromised, hence the new optical reception capability should be added without

[1] Author is with the Jet Propulsion Laboratory, California Institute of Technology.

significantly impacting the RF reflecting surfaces, the backup structure, or the pointing requirements on these operational DSN antennas. One way to achieve optical communications requirements is to polish the surfaces of the aluminum panels of the antenna's main reflector to optical smoothness, and employ a suitably large detector array to collect the focused light. However, the extent to which thin aluminum panels can be shaped and polished to optical requirements remains to be determined, along with the durability of polished surfaces in a desert environment. In addition, the antenna's ability to keep the focused spot centered on the detector array to enable optical communication remains to be quantified. This paper documents the results of experiments carried out at the Goldstone Communications Complex, to investigate and help resolve these questions.

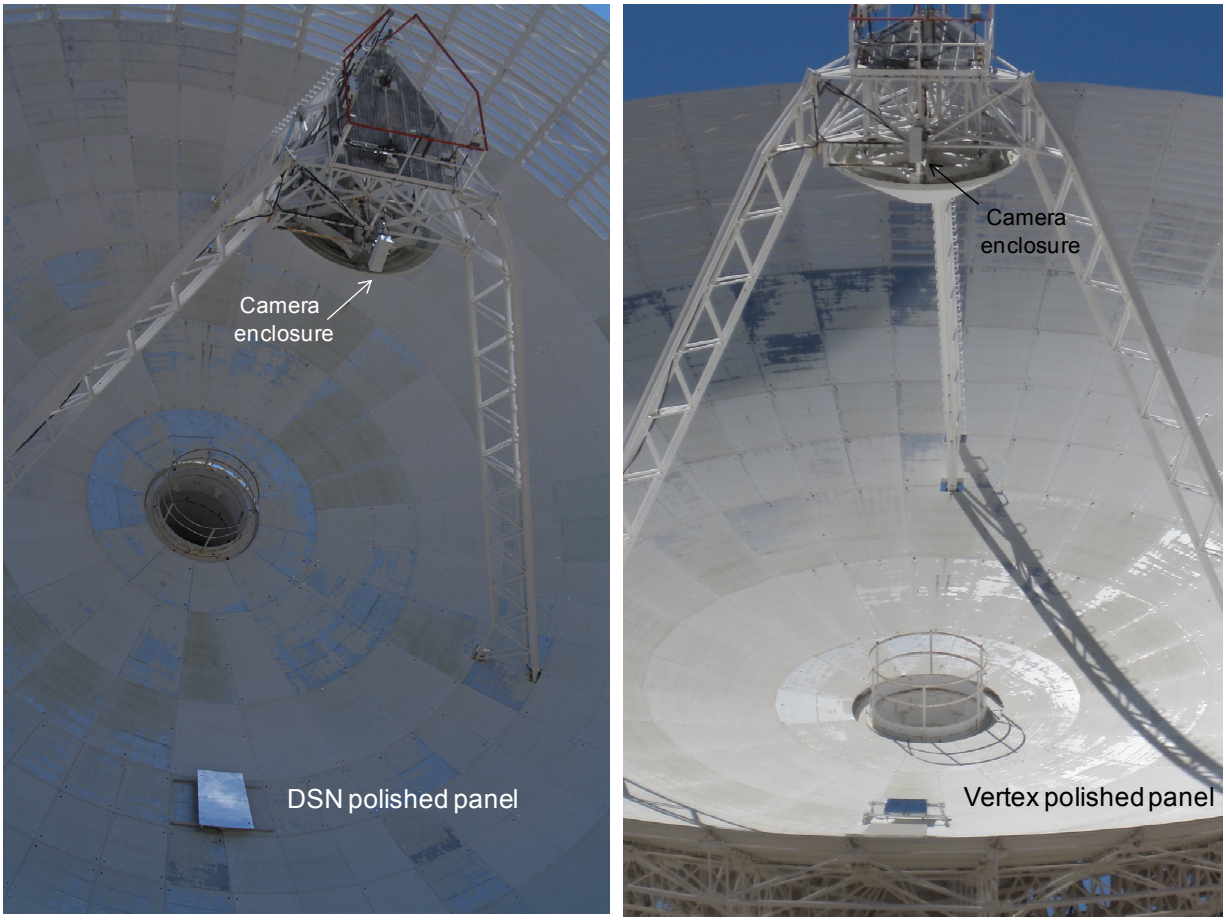

Fig. 1. DSN and Vertex Polished Panels mounted on the 34 meter research antenna at DSS-13. a) DSN polished panel mounted on the main reflector, to help establish weather and dust resistance; b) Vertex polished panel mounted on the main reflector, closer to the center. The camera enclosure can be seen next to the subreflector in both pictures.

As a first step to investigating these concepts, a spare DSN panel was polished to optical smoothness and mounted onto the main reflector of the 34 meter antenna at DSS-13 for initial evaluation of optical focusing and testing of its ability to withstand dust and rain, as well as possible oxidation of the polished surface due to long-term exposure to a desert environment. A picture of the mounted DSN polished

panel is shown in Fig. 1a, which provides an indication of the surface reflectivity, clearly showing blue sky and a small cloud reflected in the panel after several months of constant exposure. No major degradation of surface quality was observed due to oxidation, and the amount of dust collected on the panel's surface appears to have reached a steady-state value due to wind and rain, being noticeable upon inspection but not degrading reflectivity substantially, as shown in Fig. 1a. In an operational system, some means of cleaning the optical surfaces periodically will be required to maintain a desired level of reflectivity.

Next, a custom polished aluminum panel manufactured by Vertex Antennentechnic GmbH. (Germany) with prescribed curvature was procured, and mounted just inside the DSN panel as shown in Fig. 1b, in order to evaluate the PSF generated by a high quality polished aluminum panel. A 10 mega-pixel Finger Lakes Instruments (FLI) digital camera was installed in a weather-proof enclosure equipped with remote-controlled doors at each end for ventilation, and mounted next to the subreflector on the movable part of the subreflector structure, controlled from a small room located on the DSS-13 antenna (which rotates with the antenna but does not tip). A single CAT-5 cable connected from the enclosure to the room via USB-2 converters at each end, supplies power to the relays that open and close the doors, and at the same time activate the FLI camera upon command from the alidade. A picture of the mounted enclosure in the normally closed configuration is shown in Fig. 2a, tilted so as to point towards the center of the polished Vertex panel. The open configuration, used only during data-gathering, is shown in Fig. 2b where the 2" square narrowband optical filter assembly in front of the FLI camera can also be seen.

The Vertex panel was rough-aligned by measuring the distance of the sides and corners of the panel to the main reflector surface, and the camera assembly visually rough-pointed towards the center of the Vertex panel and secured in preparation for optical testing. The distance from the center of the Vertex panel to the camera sensor was determined from antenna drawings, and the camera mount placed at the nominal focal-distance of 14 meters from the center of the panel. This distance can be adjusted via subreflector commands from the control-room to fine-tune the focal distance if necessary.

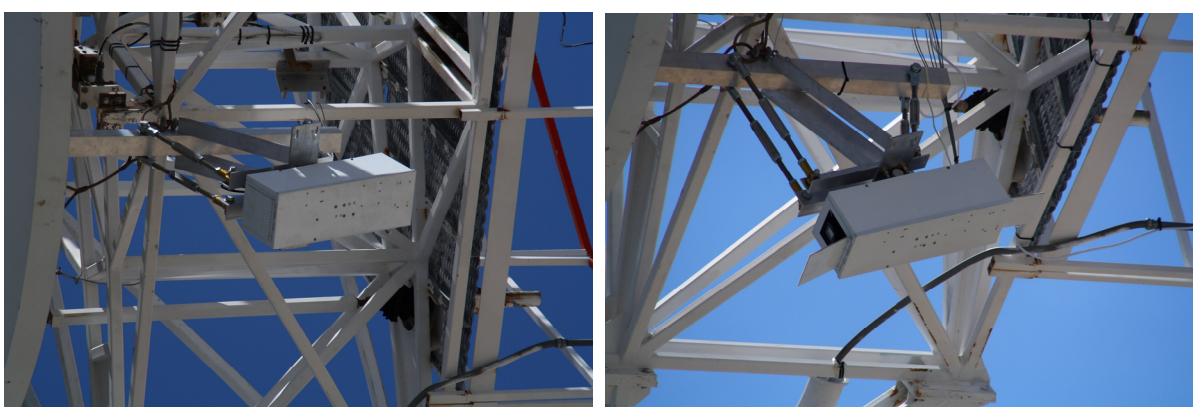

Fig. 2. Remote controlled camera enclosure: a) normally closed configuration; b) open configuration used only for data-gathering.

II. MATHEMATICAL MODEL OF FOCAL-PLANE ARRAY PROCESSING

The main goal of this data collection and processing effort is to determine how accurately the center of the PSF can be determined, in order to feed this information back to the antenna and apply the measured offsets as corrections to the nominal pointing model, thus keeping the PSF centered over the array. To facilitate analysis and derive the structure of the estimator, the sensor in the focal plane is modeled as an array of bins in Fig. 3a, and Poisson distribution assumed for the number of photo-electrons collected in each bin in response to the signal intensity, similar to the model developed previously in [1] but generalized somewhat to better accommodate the observed data. The key features of the focal-plane model are shown in Fig. 3a, which shows an elliptical intensity distribution, or "point-spread function" (PSF) in response to an optical point-source effectively at infinity such as Jupiter or a bright star. The elliptical shape was selected after it was determined that the high-quality Vertex panel generated an elliptical spot as shown in Fig. 3b.

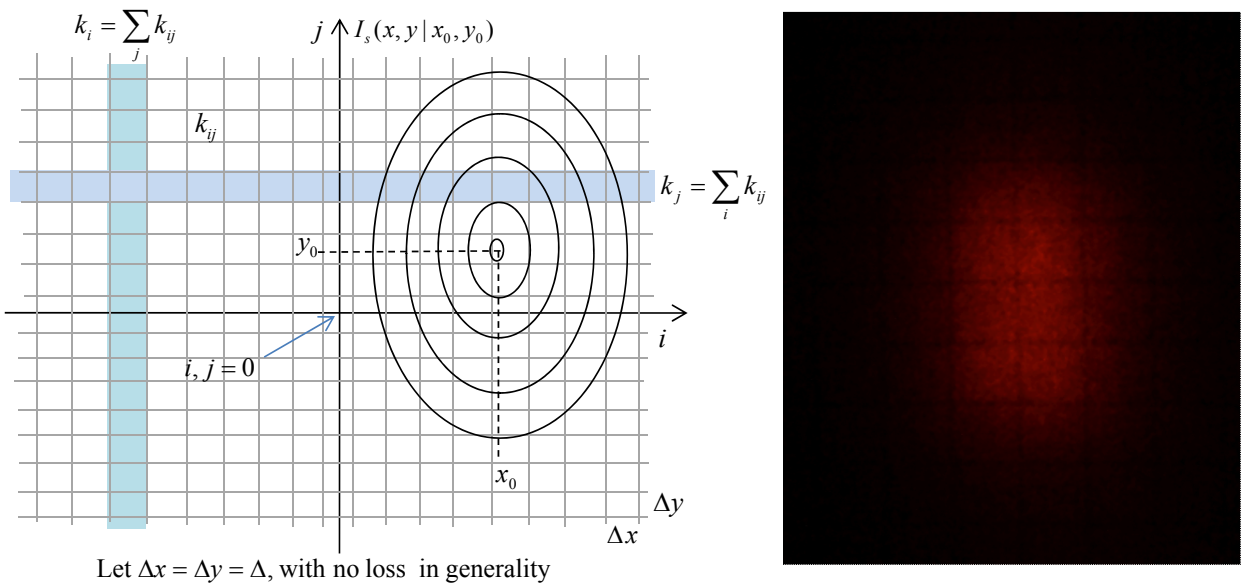

Figure 3. a) Focal-plane model of pixel array, and elliptical PSF with pointing offsets (x_0, y_0), motivated by: b) experimentally determined point-spread function (PSF) for the high-quality Vertex panel, photographed on the JPL mesa test range.

We shall assume that background radiation is negligibly small for this analysis, as indeed was the case with the Jupiter data taken at night through a narrowband optical filter. We therefore set the constant background intensity to zero: $I_b = 0$. For purposes of analysis, the PSF is assumed to be a two-dimensional elliptical Gaussian distribution as shown in Fig. 3, with center at (x_0, y_0):

$$I_s(x, y \mid x_0, y_0) = I_s\,(2\pi\,\sigma_s^2)^{-1} \exp\{-[(x - x_0)^2 / 2\sigma_x^2 + (y - y_0)^2 / 2\sigma_y^2]\} \quad \text{watts/cm}^2 \qquad (1)$$

The detector elements are small squares in this model, with power P_{ij} over the *ij* th detector-element equal to the integral of the intensity distribution over its active area. Integrating power over time yields

$$\lambda_s(i, j \mid x_0, y_0) = \int_0^T P_s(i, j \mid x_0, y_0)\, dt \cong T\Delta^2 I_s(i\Delta, j\Delta \mid x_0, y_0)$$

energy, or average "count-intensity" λ_s if the received laser energy is measured in terms of photons or photo-electrons:

(2)

With this model, the photon count from the *ij*-th detector element over a time interval of T seconds can be modeled as a Poisson distributed random variable with count probability:

$$p(k_{ij} \mid x_0, y_0) = [\lambda_s(i, j \mid x_0, y_0)]^{k_{ij}} \exp[-\lambda_s(i, j \mid x_0, y_0)] / k_{ij}! \tag{3}$$

where k_{ij} is the observed photo-count from the *ij*-th detector element. Recognizing that counts from different detector elements are independent, and defining the vector of counts from the entire array as $\mathbf{k} = \lfloor k_{ij} \rfloor$, the joint probability density of the array of counts becomes:

$$p(\mathbf{k} \mid x_0, y_0) = \prod_{i,j} [\lambda_s(i, j)]^{k_{ij}} \exp[-\lambda_s(i, j)] / k_{ij}! \tag{4}$$

Equation (4) is the starting point for deriving the maximum likelihood estimators for spatial acquisition, as well as for maximum likelihood detection of PPM symbols.

Acquisition and Tracking Performance: The derivation of the maximum likelihood estimator of the PSF offset coordinates begins by taking the natural logarithm of the conditional density defined in equation (4), which is generally called the log-likelihood function:

$$\ln p(\mathbf{k} \mid x_0, y_0) = \sum_{i,j} k_{ij} \ln[\lambda_s(i, j)] - \sum_{i,j} \lambda_s(i, j) - \sum_{i,j} \ln(k_{ij}!) \tag{5}$$

The last term is simply a constant that contains no information about the desired parameters and hence can be ignored. Note that the log-likelihood function is the log of the probability density of the count-array, conditioned on the PSF offsets (x_0, y_0). The total number of signal photons passing through the aperture in time T is designated as Λ_s. For a suitably large array that effectively contains the entire PSF, this quantity may be considered a constant independent of the offsets as in [1], yielding the simplified form

$$\ln p'(\mathbf{k} \mid x_0, y_0) = \sum_{i,j} k_{ij} \ln[\lambda_s(i, j)] \tag{6}$$

where "prime" indicates that this is no longer the logarithm of a valid probability density function, but rather a simplified version that nevertheless contains all the information needed to determine the offsets based on the observed photo-counts from the array.

For acquisition and tracking applications, we need to determine those values of (x_0, y_0) that maximize the log-likelihood function defined in equation (6). The log-likelihood function is maximized by

differentiating it with respect to the parameters of interest, setting the result equal to zero and solving, as described in [1]. This yields the following estimates $(\hat{x}_0, \hat{y}_0)$ for the PSF offset coordinates:

$$\hat{x}_0 = \Delta \sum_i i\, k_i \Big/ \sum_i \sum_j k_{ij} \quad \text{and} \quad \hat{y}_0 = \Delta \sum_j j\, k_j \Big/ \sum_i \sum_j k_{ij} \tag{7}$$

The maximum likelihood estimates of the offsets, $(\hat{x}_0, \hat{y}_0)$, are therefore seen to be the centroids of the observed count-vectors. Note that k_i is obtained by summing the counts along the index j (y-direction) for each index i (x-direction) as indicated in Fig. 3a, then using these summed counts to estimate the x-coordinate of the offset via the centroid algorithm. This is the maximum likelihood or "best possible" estimator of the x-coordinate when the statistics are Poisson, background photons are negligible and the detector array is large enough to contain all of the PSF. A similar argument holds for estimating the y-coordinate of the PSF.

Cramer-Rao Lower Bound: The Cramer-Rao lower bound on centroid estimation variance is readily derived for the case of an elliptical Gaussian intensity distribution. According to the Cramer-Rao bound, the variance of any unbiased estimator must exceed the inverse of the expected value of the second derivative of the log-likelihood function with respect to the parameter of interest. In other words, the following inequalities must be satisfied by the estimate for each coordinate:

$$\text{a) } \operatorname{var}(\hat{x}_0 - x_0) \geq \left\{ E\left[\frac{\partial^2 \ln p(\mathbf{r} \mid x_0, y_0)}{\partial x_0^2} \right] \right\}^{-1} \qquad \text{b) } \operatorname{var}(\hat{y}_0 - y_0) \geq \left\{ E\left[\frac{\partial^2 \ln p(\mathbf{r} \mid x_0, y_0)}{\partial y_0^2} \right] \right\}^{-1} \tag{8}$$

The Cramer-Rao bound is computed by first expressing the log-likelihood function explicitly in terms of the parameters of interest as

$$\ln p(\mathbf{k} \mid x_0, y_0) = -\sum_{i,j} k_{ij} [(i\Delta - x_0)^2 / 2\sigma_x^2 + (j\Delta - y_0)^2 / 2\sigma_y^2] \tag{9}$$

Differentiating twice with respect to the offsets, taking the expected value of the counts and inverting, yields the minimum attainable variance of the estimates:

$$\operatorname{var}(\hat{x}_0 - x_0) \geq \left\{ -E\left[-\sum_i \sum_j k_{ij} / \sigma_x^2 \right] \right\}^{-1} = \frac{\sigma_x^2}{\Lambda_s} \tag{10a}$$

$$\operatorname{var}(\hat{y}_0 - y_0) \geq \left\{ -E\left[-\sum_i \sum_j k_{ij} / \sigma_y^2 \right] \right\}^{-1} = \frac{\sigma_y^2}{\Lambda_s} \tag{10b}$$

Here $\Lambda_s = E \sum_i \sum_j k_{ij}$ is the total signal energy collected by the detector array. It is apparent that the variance of the coordinate estimate for each dimension is directly proportional to the squared-spread of the PSF along the given dimension, namely σ_x^2 and σ_y^2, and inversely proportional to the average number of signal photons impinging on the detector array.

In summary, the model of an elliptical Gaussian intensity distribution generating statistically independent Poisson distributed random variables in each bin of a large array, implies that the optimum estimator of the center of the PSF is a centroid algorithm applied along the x and y dimensions. The minimum attainable estimation variance can be determined by evaluating the Cramer-Rao lower bound, which suggests that the variance of the error in each dimension is directly proportional to the spread of the intensity distribution, and inversely proportional to the average number of photo-electrons generated by the signal PSF over the entire array.

Communications Performance: Following successful spatial acquisition, the PSF is centered by applying the offsets to the antenna pointing assembly, and kept centered over the detector array by means of a closed-loop tracking circuit. Temporal acquisition and tracking will commence to keep the receiver clock synchronized with the PPM symbol slot-boundaries. Under these conditions, detector array processing can be optimized to achieve best performance by sorting the array elements according to energy, and computing the symbol error probability for the highest energy bin, then the two highest, and so on, until the minimum PSE is reached. The amount of signal energy collected by the first "m" highest-energy bins will denoted by

$$K_s(m) = \sum_{n=1}^{m} \Lambda(n)$$

where "n" is the order index of the bins, according to signal energy in descending order. The background photon distribution is assumed to be uniform in the detector-plane, hence the collected background energy increases linearly with "m" as more detector elements are included. According to this model, the average number of background photons collected by the m highest-signal-energy detector elements is $K_b(m) = m\lambda_b$, where λ_b is the average background photo-count rate per detector element.

Consider the probability of correct symbol detection, with PPM signaling. For any *m*, the probability of correct symbol detection is at least as great as the probability that the photo-count in the correct slot containing the signal-pulse, exceeds the count in every other slot within that PPM symbol. To be more precise, tying equalities in (*r*-1) noise-slots (1 < *r* < *M*) should also be considered, and resolved by tossing a fair *r*-sided die, but with high average signal and background energies these events are extremely rare and hence can be ignored. With this approximation, the lower bound on the probability of correct decision, $P_M^l(C)$, as a function of *m* is given by [2,3]:

$$P_M^l(C) \geq \sum_{k=1}^{\infty} \frac{\left(K_s(m) + K_b(m)\right)^k}{k!} \exp\left[-\left(K_s(R) + K_b(R)\right)\right] \left\{ \sum_{j=0}^{k-1} \frac{\left(K_b(R)\right)^j}{k!} \exp\left[-\left(K_b(R)\right)\right] \right\}^{M-1} \tag{11}$$

$$P_M^u(E) \equiv 1 - P_M^l(C) \geq P_M(E) \cong P_M(E)$$

The corresponding symbol error probability, $P_M(E)$, is actually somewhat less than predicted by equation (11), but not significantly so. For high background cases the Poisson computations are time-intensive, and a much faster Gaussian approximation can often be used. The approximate Gaussian formula replaces the Poisson probabilities with continuous Gaussian densities whose second-order

statistics have been matched to the Poisson distribution, yielding the following equation for the probability of correct detection [2, 3]:

$$P_M(C) \cong \int_{-\infty}^{\infty} dy\, Gsn[K_s(m)+K_b(m), y]\left[\int_{-\infty}^{y} dx\, Gsn[K_b(m), x]\right]^{M-1} \tag{12}$$

Here $GSN(K,x)$ refers to the Gaussian density of the random variable x with mean and variance K. This approximation yields a somewhat pessimistic evaluation of optical receiver performance, but it is nearly exact for the case we are considering, and also helps to provide insights into the behavior of key design parameters in communication applications.

III. Jupiter Observation: Data Acquisition and Signal Processing

After installing the camera assembly and routing the control cable to the antenna's alidade, the camera enclosure was activated remotely and nominal operation of the entire system verified. The enclosure was designed to withstand desert heat, rain and wind with the aluminum doors closed as shown in Fig. 2a, and to quickly cool down during operation with both doors open (Fig. 2b). Although the assembly is always connected to AC power available on the subreflector backup structure, the camera and all power supplies are connected through relays, which in turn are controlled remotely from the alidade via USB-2 extenders at each end connected via a durable CAT-5 cable running from the alidade through the main reflector and routed through the leftmost tripod in Figs. 1a and b. Since the doors are computer controlled via relays, the entire unit is powered up when the doors are commanded to open: otherwise, there is no AC power reaching the internal components. The entire enclosure has been painted glossy white, and shown to successfully resists heating even in direct sunlight.

Following confirmation of basic remote control and camera functions, the next step was to determine the antenna pointing offsets required to place the focused optical image of a celestial source directly onto the camera's filter assembly: the moon was selected for initial alignment, since its focused image could be seen directly on the closed door of the enclosure. A nearly full moon was used to attain initial alignment, by carefully placing the center of the roughly circular image over the location of the camera within the enclosure. Next, the antenna was re-pointed to Jupiter which was rising in the east and the offsets applied, however Jupiter's image could not be seen directly on the enclosure door even with powerful binoculars. The doors were activated and a 1-second exposure was made with the FLI camera, which registered a faint signature near the top of the image. Longer exposures confirmed the presence of a bright signature, which was used to refine the pointing offsets, centering the Jupiter signature on the sensor.

Data collected during the first Jupiter observation (July 19th, 2011) consisted of FITS files with 3084X3103 array elements, quantized to 16 bits. The control software of the FLI camera thresholds the pixel values at approximately 2000 out of a total of $2^{16} = 65536$, in order to overcome dark current and other instrument effects. Photo-electrons generated by the signal are added directly to this value, producing

photo-counts in the 2000-2400 range, as can be seen in Fig. 4a. This lower threshold value was subtracted before binning, hence the binned intensities shown in Fig. 4b range from zero to a high value of 180. These images represent accurate estimates of the PSF generated by the Vertex panel, hence we proceed to evaluate tracking and communications performance of a future optical communications system based on the images obtained by the FLI MicroLine 9000 camera.

A large number of Jupiter images were recorded, starting with centered images followed by images with small pointing offsets, in order to characterize the response of the panel. Offsets ranging from 25 mdegs to 100 mdegs were applied in both EL and XEL, in order to facilitate the evaluation of centering algorithms and communications performance. False-color images of the Vertex polished panel's response to Jupiter are shown in Figs. 4a and b. Both the original 10-mega-pixel image, and a processed version where the pixels were binned into 60X60 pixel subarrays with intensity averaging, resulting in an array of 50X50 bins. Upon closer inspection of the data, it was noted that the first row and first column of the array contained much less signal energy than the rest (likely due to masking of the sensor by the inner edge of the filter assembly), hence the first row and column were deleted resulting in a 49X49 element array. No PSF information is lost since the extent of the PSF is much greater than the size of the bins hence it is sampled adequately in both spatial dimensions.

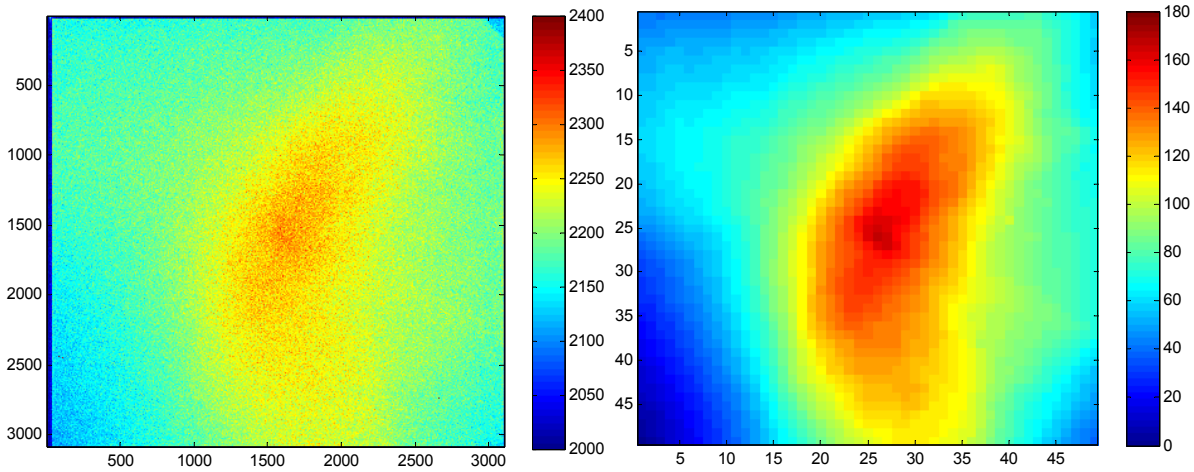

Fig. 4. Centered PSF recorded by FLI camera: a) original 10 mega-pixel resolution showing speckle pattern; b) binned image emphasizing the spatially averaged structure of the point-spread-function.

The salt-and-pepper appearance of the original image in Fig. 4a is believed to be a speckle pattern averaged over the integration time, similar to that produced by a laser, for the following reason. Note that the brightest region in the binned PSF shown in Fig. 4b corresponds to the region with the greatest number of high-intensity speckles in the original image, and is approximately 10X15 bins in extent. Note that the spots obtained in these experiments are significantly more distorted than the elliptical spots photographed on the JPL mesa test-range, likely due to mechanical distortion.

When the detector elements are sorted according to signal energy, the distribution of energies shown in Fig. 5a is obtained as a function of the order index "n". Note that all of the 2401=49X49 detector elements contain some signal energy, falling off with increasing order index n.

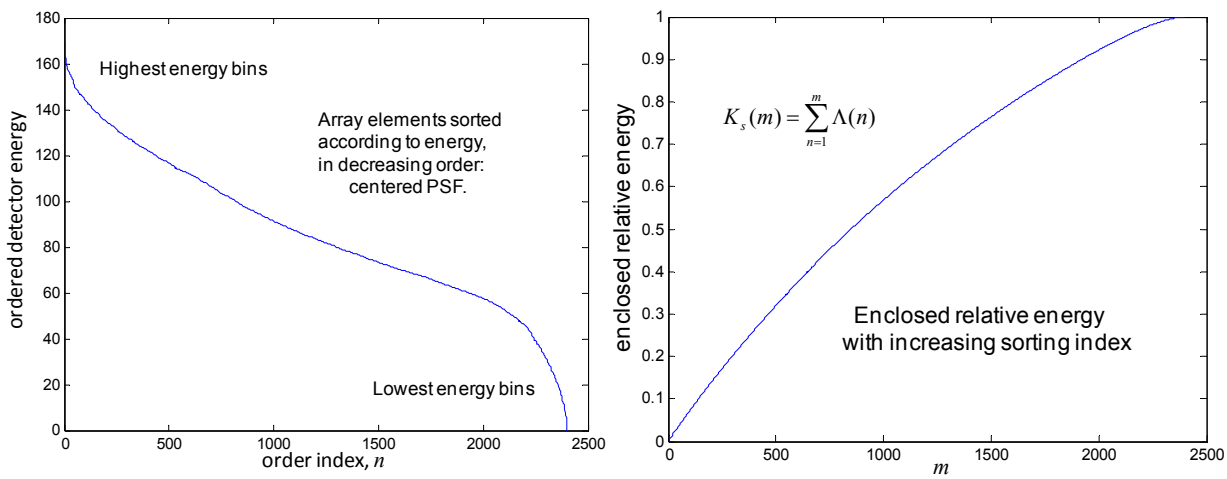

Fig. 5. a) Detector elements sorted according to energy, for a centered PSF; b) Accumulated relative energy in the first "m" sorted detector elements.

From the viewpoint of optical communications, the most important criterion is detecting and decoding the transmitted data with high fidelity: this implies the use of advanced detection strategies to achieve the lowest possible symbol-error probabilities consistent with the prevailing operating conditions. As shown in [2], optimal processing of photon-counting detector array data requires optimal weighting of the array elements by a logarithmic factor $w_{ij} = \ln(1 + \frac{K_s}{K_b})$, which may be difficult to compute and apply in a practical implementation when a large number of detector elements are involved. However, it was also shown in [2, 3] that a simple "1, 0" mask that selects the most favorable detector elements and rejects the rest achieves nearly the same performance as the more complicated optimal weighting strategy. We shall proceed to analyze both acquisition and symbol-detection capabilities of a hypothetical optical receiver employing the Vertex panel as the collecting aperture, and a photon-counting array with elements corresponding to the binned subarrays of the large-sensor FLI camera.

Symbol Error Probability for Offset PSF: Assuming the intensity distribution obtained from the camera is a reasonable representation of the average PSF generated by the Vertex polished panel, we proceed to evaluate communications performance for pulse-position modulation (PPM) with 4 slots per symbol, as described in [1]. We consider a case where the antenna has been nominally pointed towards the source based on pre-computed pointing predicts, but due to unmodeled effects such as uneven solar heating that may have caused thermal gradients across the antenna, the PSF is not centered but appears 100 mdegs too high, in the upper half of the detector array as shown in Fig. 6a.

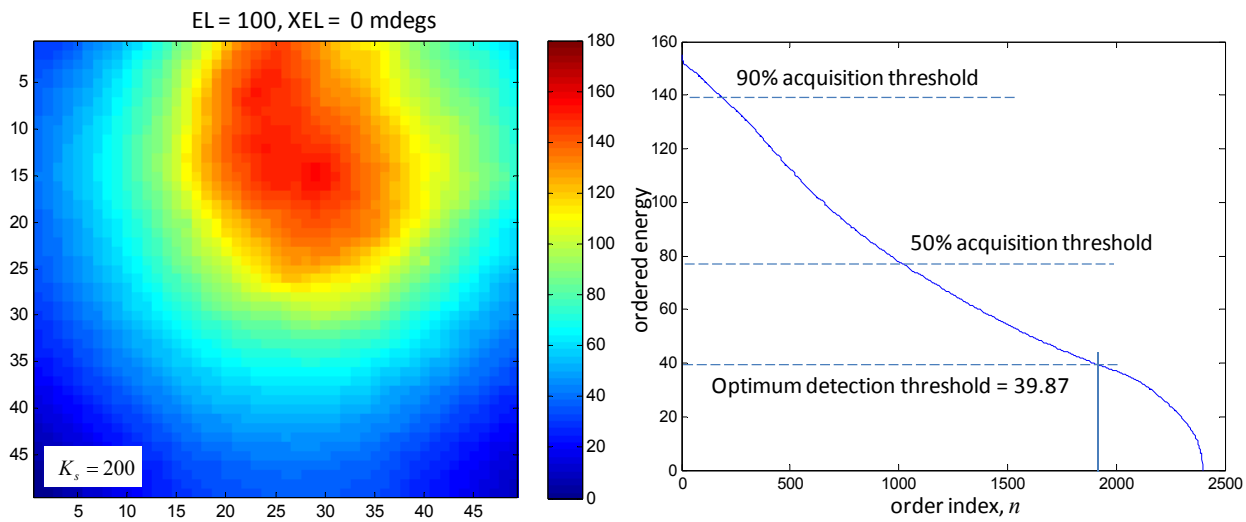

Fig. 6. a) Initial PSF before centering, showing 100 mdeg pointing error in elevation; b) Detector elements ordered according to intensity, as a function of the order index "n".

As a first step, the array elements are ordered according to intensity as in Fig. 6b, where "n" is the index of the ordered intensity. The total energy contained in the "m" highest intensities as a function of m, is shown in Fig. 7a for the offset PSF. The PPM symbol-error probability, PSE, has been obtained for this case as a function of m by evaluating equation (12) assuming four slots per PPM symbol so that M=4, assuming total average signal energy of $\Lambda_s = 200$ photons distributed according to the PSF (a reasonable estimate of symbol energy according to the analysis in [1]), and a constant average background count of $K_b = 0.3$ photons per detector element. The computed symbol error probability is shown in Fig. 7b as a function of m, where it can be seen that PSE is minimized by selecting the 1900 highest-intensity pixels. Note that for this example, nearly all of the signal energy contained within the PSF must be summed in order to minimize the symbol-error probability.

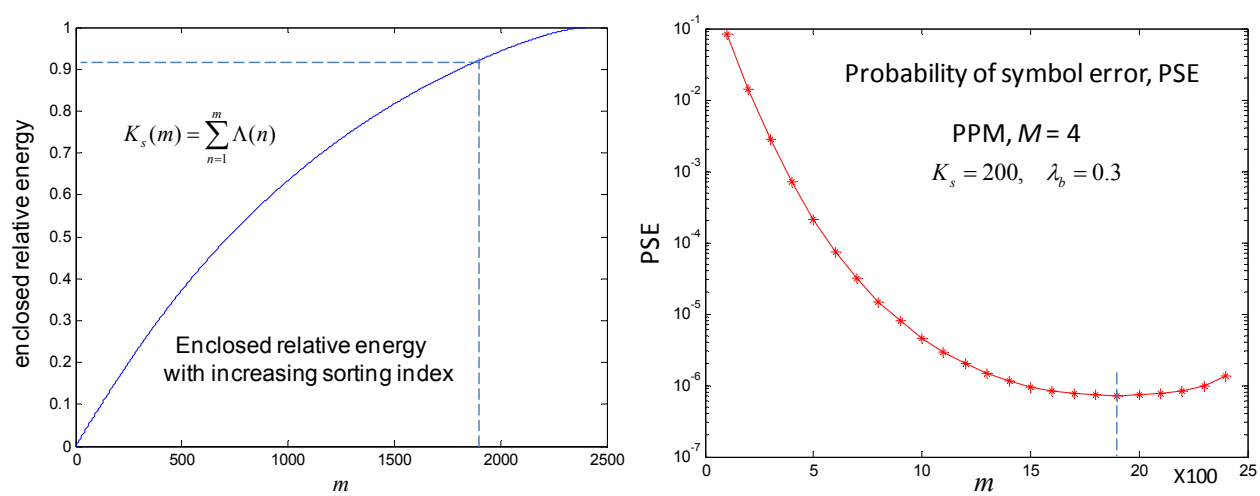

Fig. 7. a) Accumulated relative energy as a function of the "m" highest intensities; b) symbol error probability PSE as a function of m, showing the minimum at m=1900;

The application of the detection threshold defined in Fig. 6b to the array is equivalent to generating a simple "1, 0" mask, that in effect determines which detector elements are to be included in the detection operation: a point-by-point array multiplication excludes the unwanted array elements, which contain too little signal energy to help with detection, hence would contribute too much noise and cause the symbol error probability to start increasing, as in Fig. 7b) for $m > 1900$. The "1, 0" detection mask for this off-center case is shown in Fig. 8a, along with the modified intensity distribution resulting from the application of the detection mask to the offset intensity distribution.

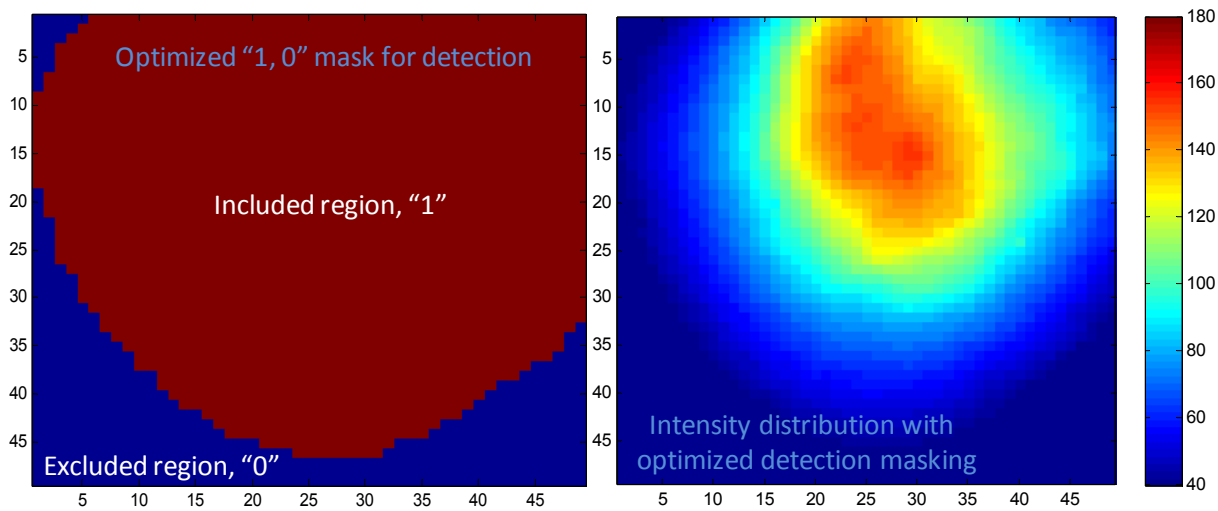

Fig. 8. a) Simple "1, 0" mask obtained by including only those elements with order index less than 1900; b) modified intensity distribution after the detection mask is applied.

Acquisition Algorithms and PSE for Centered PSF: Since the PSF is not centered in the above example, some of the signal energy falls outside the array, and hence does not contribute to signal detection as can be seen in Figs. 6a and 8b. The total signal energy per pulse over the array was taken to be 200 photons in the above example, but it is clear that this signal energy could be increased by re-centering the PSF over the array. Ideally, the centering operation consists of determining the coordinates of the PSF center as described above, applying the offsets determined by the centroid algorithm to the antenna pointing assembly, and re-pointing the antenna to center the PSF over the detector array.

The derivation that led to the centroid algorithm assumed a suitably large detector array where edge effects were not significant, however that is clearly not the case in this example, even though the PSF can be reasonably approximated by an elliptical distribution. The problem is that as signal energy is lost over the top edge of the array, the estimate of the centroid algorithm becomes biased towards the center since there is a point where the signal energy in the lower half of the array compensates for the signal energy lost over the edge. This effect can be seen in Fig. 10b, where direct application of the centroid algorithm defined by equations (10a) and 10b) results in center-coordinate estimates $(\hat{x}, \hat{y})$ that are clearly biased towards the center of the array, significantly missing the highest intensity regions of the PSF which are of greatest interest.

In an attempt to improve the estimates for point-spread-functions suffering from unmodeled edge-effects, the centroid was re-computed after the application of the detection mask, since it is this region that should be centered over the array for best communications performance. These new estimates are denoted as $(\hat{x}_d, \hat{y}_d)$ in Fig. 10b, yielding noticeably better results since now part of the signal energy in the lower half of the array is zeroed out by the detection mask as shown in Figs 8a and b, hence these bins do not contribute to the centroid algorithm. It is clear from Fig. 10b that application of the detection mask to the signal intensity distribution improved the estimate of the PSF center, and that repeated application of these estimates to antenna pointing will eventually center the PSF, however a faster "one-step" method would be useful to help acquire the signal quickly and center it over the array, even if there were significant initial offsets in antenna pointing.

We observed that the centroid algorithm as applied to the original distribution, using all 2401 array elements, yielded y-coordinate estimates that were strongly biased towards the center. However, after applying the detection mask only those intensities above the "detection threshold" in Fig. 7b were used to compute the centroid, resulting in noticeably better estimates. It is natural to ask if even better estimates could be obtained by raising the threshold still further, determining the resulting mask, and applying it to the array before computing the centroids. Therefore, masks corresponding to the 50% and 90% intensity thresholds were generated (see Figs 9a and 10a), yielding greatly improved estimates $({}_{50}\hat{x}_{th}, {}_{50}\hat{y}_{th})$ and $({}_{90}\hat{x}_{th}, {}_{90}\hat{y}_{th})$ by these "modified centroid algorithms" as shown in Fig. 10b. Note that we are not using the assumed signal energy of 200 photo-counts to compute the centroid at this point, as we had to in order to compute performance, but only the average energy distributions of the PSF defined by the data to compute the centroids. The effects of signal energy on the ultimate accuracy of the estimates will be considered in the last section, where the limits imposed by the CRB will be seen to depend on the energy in the signal pulse.

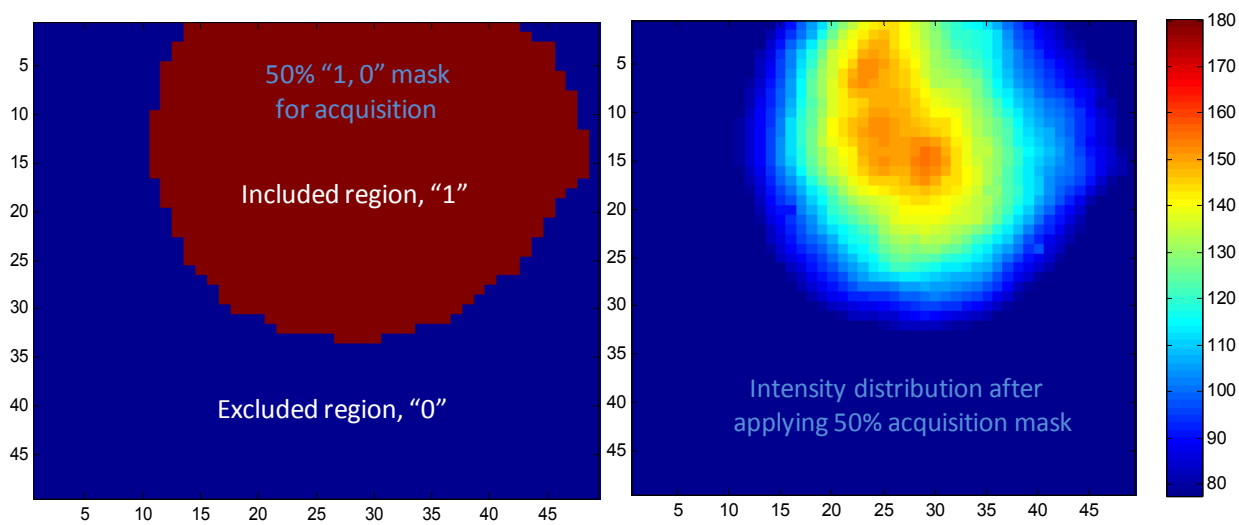

Fig. 9. A) "1, 0" acquisition mask corresponding to 50% threshold; b) resulting intensity distribution after acquisition mask is applied.

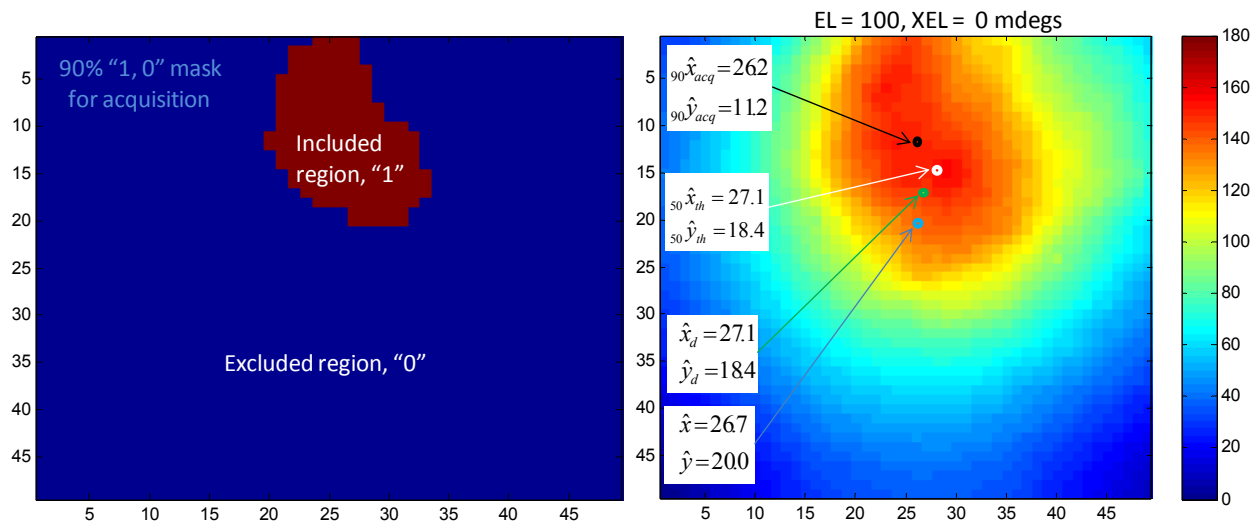

Fig. 10. a) "1, 0" acquisition mask corresponding to 90% threshold; b) PSF center estimates obtained with the original centroid algorithm, detection-mask modified algorithm, 50% and 90%-threshold algorithms.

Raising the acquisition threshold still further eventually converges onto the single bin with the greatest energy, however it is not clear that centering the highest-energy bin is the best strategy, since that bin may be near the edge of the distribution in some cases. Care must be exercised to center the PSF in such a way as to maximize the signal energy collected by the array, consistent with the detection mask for the centered distribution. The best acquisition threshold remains to be determined, but will likely consist of using a threshold much higher than the detection threshold for initial acquisition, followed by a lower threshold for real-time closed-loop tracking, thus ensuring that detection performance remains optimized.

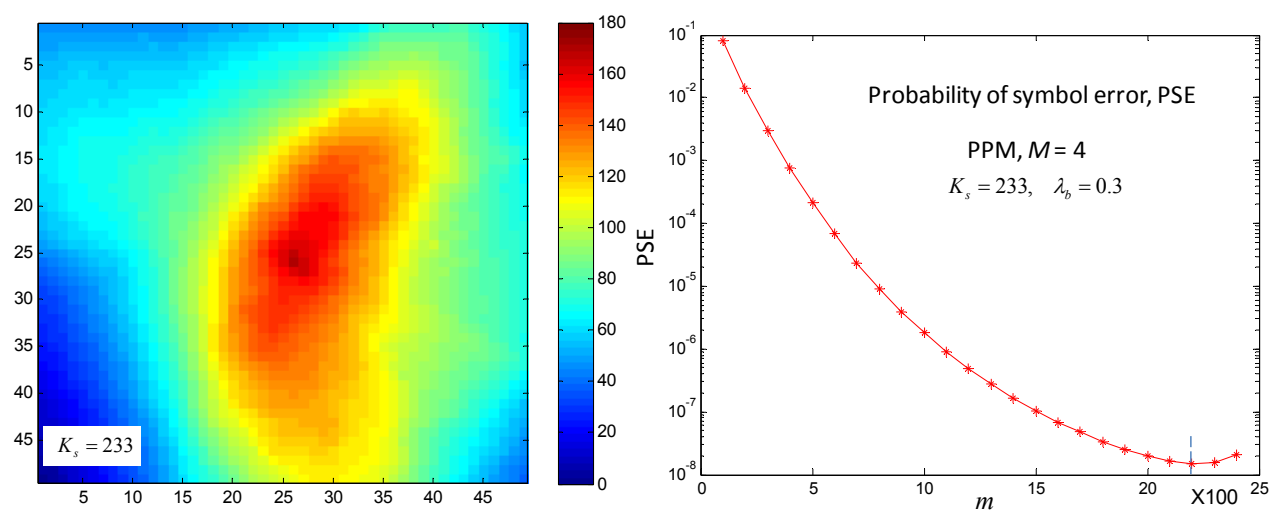

Fig. 11. Detection performance of centered PSF: a) binned image representing total average signal count of 233 photons; b) probability of symbol error with optimal "1, 0" mask, for average background counts of 0.3 photons per slot per bin.

The symbol error probability was recomputed for the centered PSF case, in order to quantify the improvement provided by the centering operation. Indeed, it was found that by increasing the signal energy in proportion to the measured energies yielded 233 signal photons for the centered PSF, improving the "0,1" optimized detection performance from $PSE = 10^{-6}$ in the off-center case (Fig. 7b), to $PSE = 1.5 \times 10^{-8}$ for the centered case, as can be seen in Fig. 11b. It should be noted that the optimum value of m has now increased from 1900 to 2200, due to the generally higher level of signal energy throughout the array.

Comparison of Modified Centroid Algorithms: The original unmodified centroid algorithm, along with the modified 50% and 90%-threshold versions were evaluated on the Jupiter data collected on July 19th , 2011. Offsets of 25 mdegs, 50 mdegs and 100 mdegs were applied to the antenna pointing, and the response of the test setup consisting of the Vertex polished panel and camera sensor array were recorded. The centroid estimates for the original unmodified centroid estimator were recorded in each case, along with the 50% and 90% modified centroid estimators. These results are presented in Figs. 12a-f and 13a-f, for elevation offsets of ± 100 mdegs, and cross-elevation offsets of ± 50 mdegs (the -50 mdeg elevation data-set was missed during data-collection, hence the 100 mdeg elevation data is presented instead) . Note that there is obvious coupling between elevation and cross-elevation when the cross-elevation offsets are applied to the antenna, shown in Figs 12d-f and 13d-f; this is likely due to a slight tilt in the polished panel. It can also be seen in Figs. 12a-c and 13a-c that the response of the panel to elevation offsets is not symmetric: with 100 mdeg elevation applied the PSF moves a little more than half way up on the sensor, but -100 mdeg elevation offset moves the center of the PSF completely off the sensor, so that only the tail of the distribution can be seen. A triangular intensity artifact can also be seen in c) and f) of both figures, due to reflections from the inside edge of the filter assembly: a mask has since been place in front of the filter assembly, which should eliminate this problem in future data. The remaining asymmetries and coupling in the response will likely be reduced after the tilt of the polished panel is refined to eliminate the large elevation offset of 7.125 degrees in antenna pointing.

It is clear that both acquisition algorithms yield better results than the original unmodified centroid algorithm, due to the fact that the actual detector array is not much larger than the PSF, and also due to pointing-dependent changes in the PSF that were not modeled. The 90% threshold algorithm provides estimates that are visibly close to the brightest part of the PSF in all cases, and therefore will tend to re-center the PSF quicker, if large initial offsets are present. This modified algorithm necessarily tracks a smaller signal intensity distribution around the peak, hence it is less susceptible to asymmetries and distortions, but also contains less energy and hence will operate with larger estimation errors.

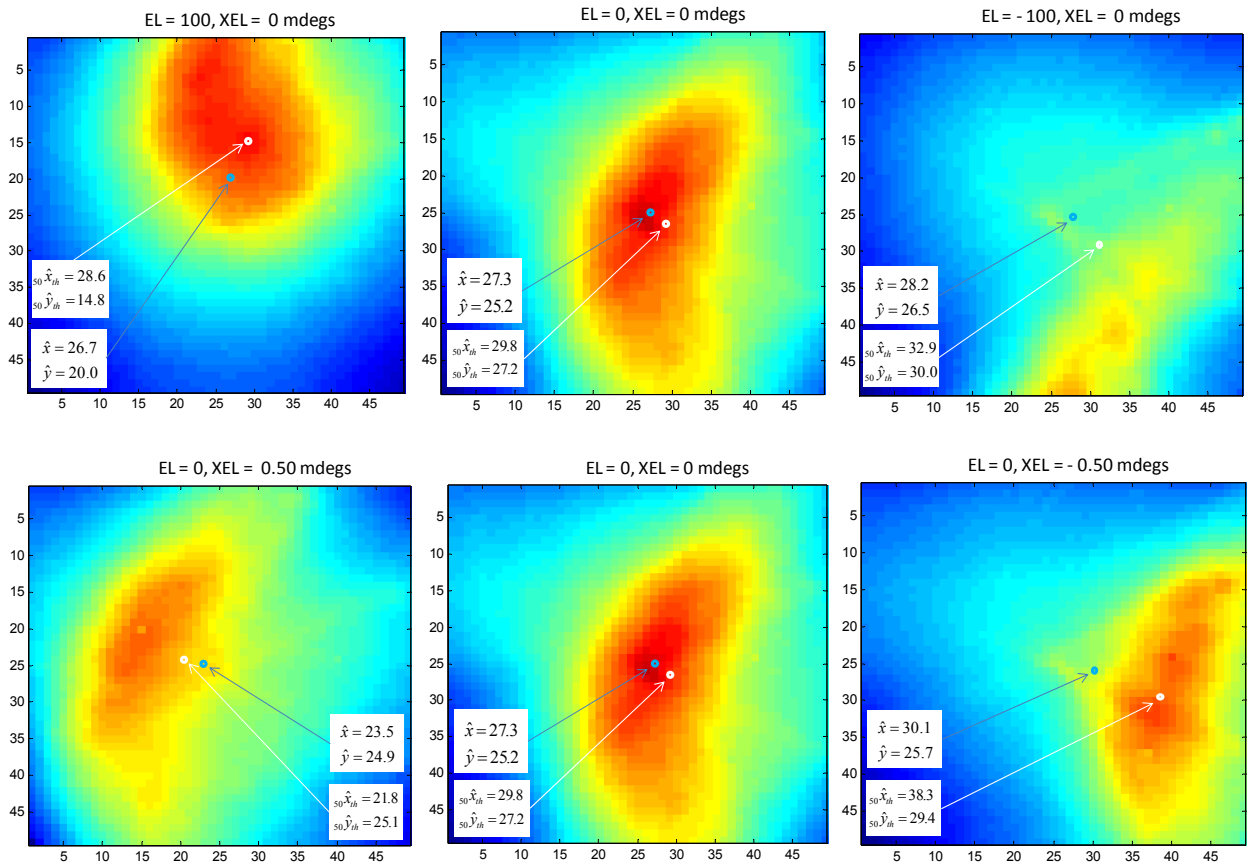

Fig. 12 Original and 50%-threshold estimates, with elevation and cross-elevation offsets: a) EL = 100 mdeg; b) EL = 0 mdeg (centered); c) EL = -100 mdeg; d) XEL=50 mdeg; e) XEL = 0 mdeg (centered); f) XEL=-50 mdegs.

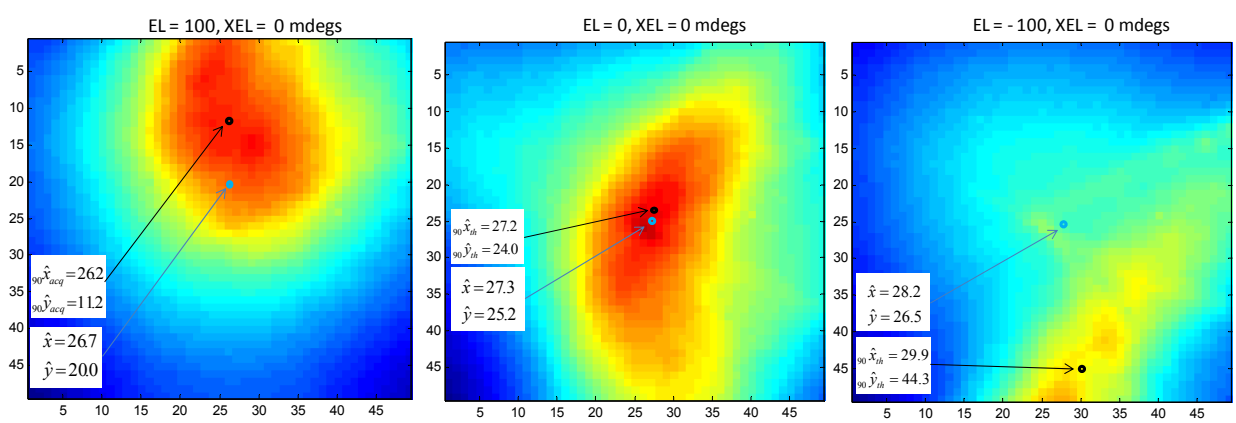

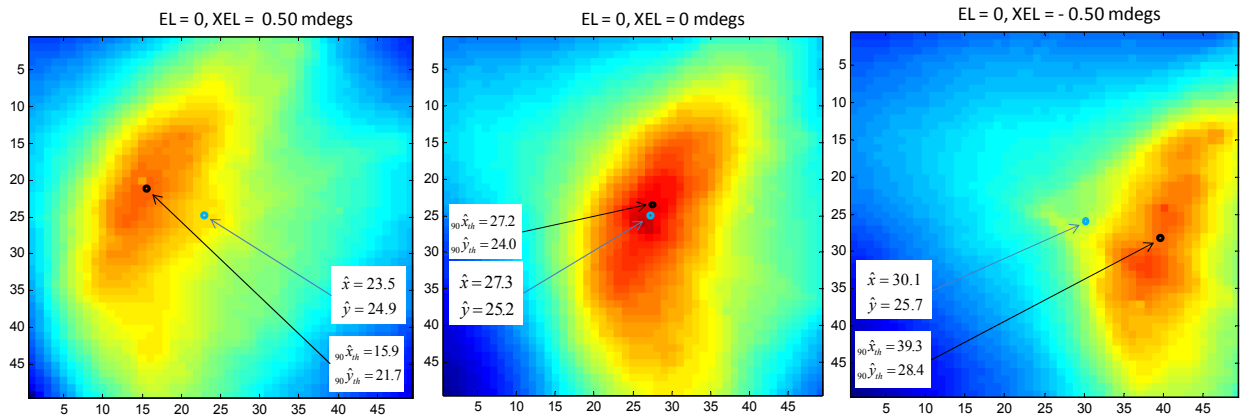

Fig. 13. Original and 90%-threshold estimates, with elevation and cross-elevation offsets: a) EL = 100 mdeg; b) EL = 0 mdeg (centered); c) EL = -100 mdeg; d) XEL=50 mdeg; e) XEL = 0 mdeg (centered); f) XEL=-50 mdegs.

The results of the original unmodified centroid algorithm, and modified 50% and 90%-threshold algorithms are summarized in Table 1, where it can be seen that all three centroiding algorithms provide estimates with the correct sign, hence are theoretically capable of re-centering the PSF after sufficiently many steps. However, the 50% and 90%-threshold algorithms provide estimates with greater magnitudes, implying that the centering operation will take fewer steps to accomplish. Since all three algorithms yield similar estimates for the centered PSF, the estimates of the off-center cases were measured relative to the center coordinates provided by that algorithm: therefore a row of zeros, designated "del-center", was included in the table to emphasize this point.

	$\hat{x}$	$\hat{y}$	${}_{50}\hat{x}_{th}$	${}_{50}\hat{y}_{th}$	${}_{90}\hat{x}_{th}$	${}_{90}\hat{y}_{th}$
center	27.3	25.2	29.8	27.2	27.2	24.0
$\Delta - \text{center}$	0	0	0	0	0	0
EL=100	-0.6	-5.2	-1.2	-12.4	-1.0	-12.8
EL=-100	0.9	1.3	3.1	2.8	2.7	20.3
XEL=50	-8.0	-2.3	-8.0	-2.1	-11.3	-2.3
XEL=-50	2.8	0.5	8.5	2.2	12.1	4.4

Table 1. Summary of center estimates, and response to "large" offsets relative to center for the original, 50% and 90%-threshold centroid algorithms.

Following initial acquisition and initial centering of the PSF over the array, the detection mask is applied and temporal synchronization begins, followed by symbol-detection and decoding of the received data.

Acquisition is now replaced by tracking, whereby the detection mask is maintained over the array to continuously facilitate symbol detection. Since tracking implies the correction of small changes in pointing, the original unmodified centroid, and 70%-threshold and 90% threshold centroid algorithms were evaluated for smaller ± 25 mdeg elevation and cross-elevation offsets. The results are shown in Table 2, where it can be seen that all three algorithms respond to the smaller offsets, but the unmodified algorithm is not consistent for XEL=-25 mdegs, due to the fact that the shape of the PSF dominates the centroid over such small displacements. However, both the 70% and 90%-threshold algorithms provide consistent estimates that should keep the PSF centered over the array, with the 70% showing very good response in EL, and somewhat less cross-coupling in XEL than the 90% threshold algorithm.

	$\hat{x}$	$\hat{y}$	${}_{70}\hat{x}_{th}$	${}_{70}\hat{y}_{th}$	${}_{90}\hat{x}_{th}$	${}_{90}\hat{y}_{th}$
center	27.2	25.1	29.8	27.2	27.3	24.0
$\Delta - \text{center}$	0	0	0	0	0	0
EL=25	-0.5	-1.1	-1.3	-3.1	-0.3	-1.9
EL=-25	0.0	0.6	-0.3	4.3	1.0	4.8
XEL=25	-3.0	-1.5	-8.7	-4.5	-4.4	-2.3
XEL=-25	0.0	-0.8	2.5	0.8	5.6	3.6

Table 2. Summary of center estimates, and response to "small" offsets relative to center for the original, 70% and 90%-threshold centroid algorithms.

The response of the 90%-threshold algorithm to large offsets, and that of the 70% algorithm to small offsets are shown in Figs. 14, represented as points on the (XEL, EL) plane. Cross-coupling between the elevation and cross-elevation offsets is evident in this representation, manifested by non-orthogonal response in the two orthogonal directions, and likely caused by panel tilt and stress. Note that in addition to cross-coupling, the response to elevation offsets in the positive direction is greater than in the negative direction, again likely due to panel tilt and distortion. Interestingly, the response of the 70% threshold algorithm to small offsets in the cross-elevation direction seems to be less symmetric, with greater cross-coupling than in the elevation direction.

The major impact of non-orthogonal response is that the PSF cannot be centered in a single step in general, since a given offset in one direction (elevation or cross-elevation) results in a PSF displacement in both directions, hence the antenna will be commanded to apply an offset in both directions instead of just one, causing a smaller coupled offset that also has to be corrected in a following step. A possible trajectory for two-step acquisition by the 90%-threshold algorithm is shown in Fig. 14a, illustrating the process. Let's assume that 100 mdeg displacement corresponds to 20 detector-elements over the array, as shown in Fig. 14a. We know that when the 100 mdeg offset in elevation is removed, the PSF returns

to its centered position at (0, 0) in the (XEL, EL) plane, since this was confirmed repeatedly during the experiment. However, based on the measurement, the antenna will be commanded to move not only 20 units in the negative-EL direction, which would place it back to (0,0), but also 2.5 units in the negative XEL direction, placing it 2.5 units on the negative XEL axis, instead of the origin. This point is shown as a red dot located at point "a" (XEL=-2.5, EL=0) in Fig. 14a. This new location will register a small cross-elevation offset, which will be applied to the antenna pointing during the next step, incurring a slight positive error in elevation at point "b", due to the error introduced by cross-coupling. Since this remaining error is small compared to the PSF it can probably be ignored, or another step could be applied to remove the residual elevation error, leading to an iterative solution.

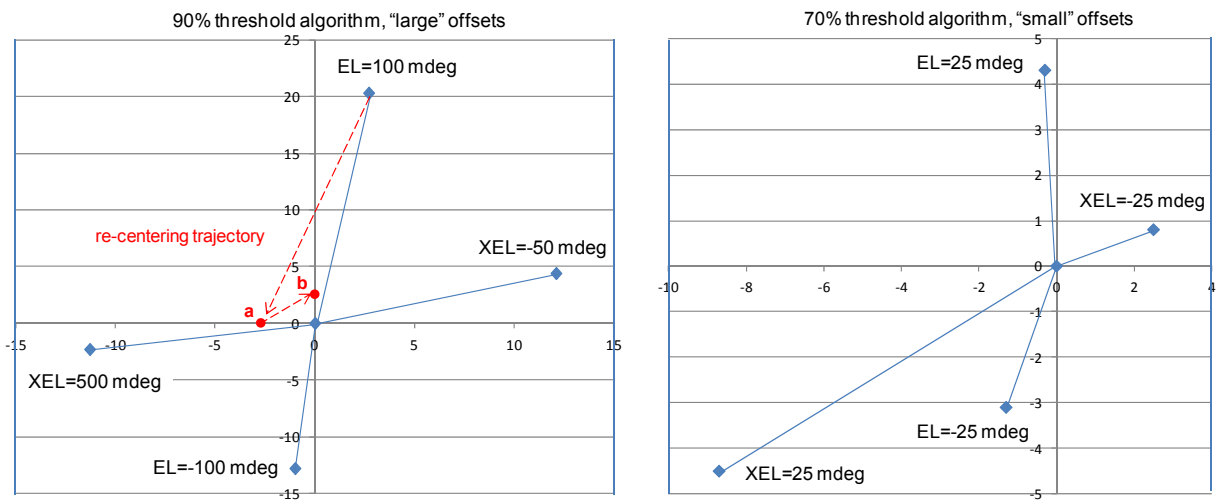

Fig. 14. Response of a) 90%-threshold algorithm to "large" offsets, and b) 70%-threshold algorithm to "small" offsets, in the (XEL, EL) plane.

The response of the 70% threshold algorithm to small offsets is shown in Fig. 14b, indicating even greater cross-coupling when XEL offsets are applied, and asymmetrical response to positive and negative offsets. It is believed that removing the tilt from the polished panel and reducing stress as much as possible will tend to ameliorate these effects.

Fundamental Limits on Centroid Estimator Performance: When attempting to measure and resolve small offsets, the inherent ability of the estimators should be determined, to make sure that the resolution requirements can be met under realistic operating conditions. The Cramer-Rao bound (CRB) is important in determining the lower bound on the estimation error that any unbiased estimator can achieve, hence we proceed to evaluated the CRB for the communications examples considered above, and shown in Fig. 15. Taking the effective spread of the PSF in the x and y directions, σ_x and σ_y respectively, to be 12 and 16 array-elements, and assuming a PPM symbol energy of 200 photons in the EL = 100 mdeg offset case as before, the CRB has been determined using equations (10), and plotted as small error ellipses in Fig. 15 for the unmodified centroid algorithm that uses the entire PSF, and the 90%-threshold algorithm that uses only the highest energy regions to compute the centroid.

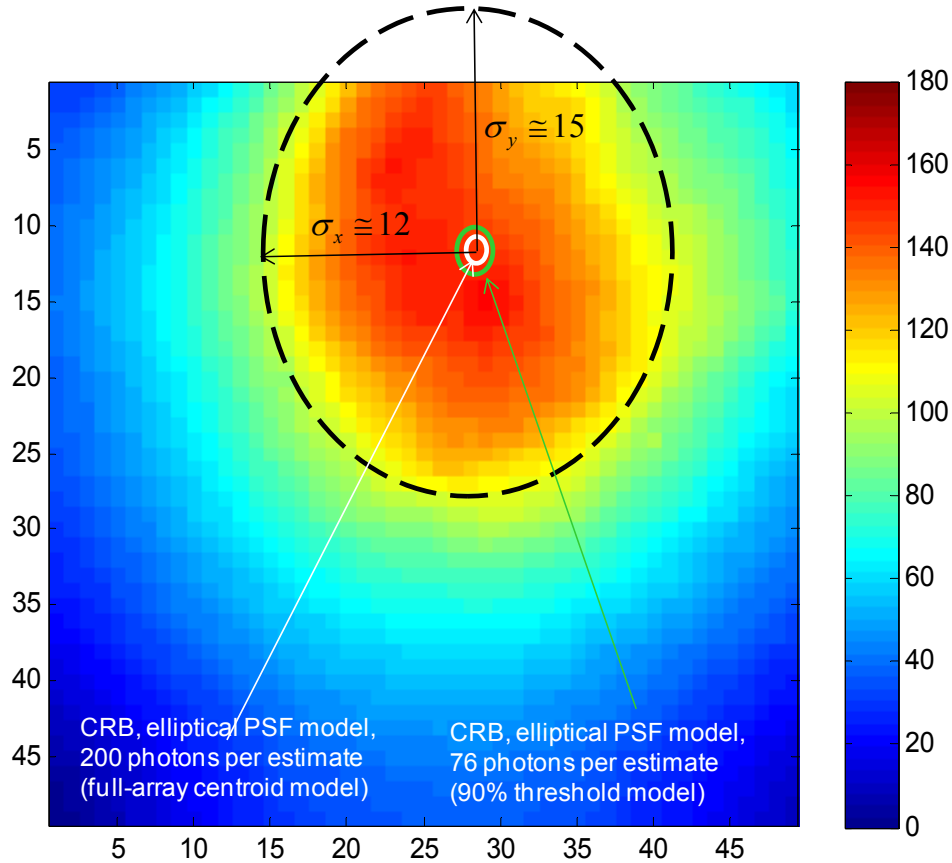

Fig. 15. a) Estimate of the Cramer-Rao bound for the unmodified and modified threshold algorithms: elliptical PSF with minor axis ~12 bins, major axis ~16 bins.

Substituting $\sigma_x^2 = 144$, $\sigma_y^2 = 256$ and $\Lambda_s = 200$ into equations (10) yield the minor and major axes of the Cramer-Rao bound as 0.85 and 1.1 bins, respectively. Similarly, the signal energy for the 90% threshold mask was approximately 76 photons on the average: letting $\Lambda_s = 76$ in equations (10) yields CRB-ellipse minor and major axes of dimensions of 1.4 and 1.8 bins, respectively, still much smaller than the relevant dimensions of the PSF.

Similar results were obtained for the centered, and slightly off-center cases as well. It appears that any algorithm that approaches the CRB will be able to measure both large and small offsets with close to one element resolution, even if only the minimum energy of a single PPM symbol is used to make these estimates, which would require slot-synchronization and some idea of where the markers are, but that is not unreasonable since temporal synchronization can be established even with an offset PSF before spatial acquisition, if enough signal energy is present. This enables the use of frame markers or other known symbol patterns to be used for the tracking operation once symbol-sync has been determined, even if these markers occur at a rate much lower rate than the data, to keep the PSF centered over the array. We conclude that under nominal operating conditions the estimation error will typically be much smaller than the PSF, and estimation errors will likely be dominated by asymmetries and artifacts due to panel imperfections, rather than the fundamental limit on estimation error imposed by the CRB.

IV. SUMMARY AND CONCLUSIONS

Installation and initial evaluation of polished aluminum panels intended for optical communications via hybrid 34-meter DSN antennas has been described in this paper. It was shown that high-quality aluminum panels can be manufactured with surface accuracies sufficiently accurate to concentrate light into small, roughly 1 cm spots, that could be detected with large area photon-counting arrays. As part of this demonstration effort, an aluminum panel manufactured by Vertex Antennentechnic GmbH. was installed on the main reflector of the 34-meter antenna at DSS-13, and a large-sensor camera manufactured by Finger Lakes Instruments simulating a future large-area photon-counting array, was installed into a weather-proof enclosure and mounted next to the subreflector to record the point-spread function (PSF) generated by the polished panel. Data was collected while tracking the planet Jupiter at night, which provided sufficient illumination to produce detailed images of the PSF with various antenna pointing offsets, facilitating the evaluation of algorithms designed to acquire and track the PSF, as well as evaluation of future communications performance. A detailed mathematical model of the focal-plane energy distribution was developed, algorithms designed to estimate the centroid of the PSF were derived based on optimum estimation theory, and performance limits established via the Cramer-Rao bound. The theoretically derived algorithms were modified to take into account unmodeled features in the recorded data, and shown to provide accurate enough estimates of PSF coordinates to enable acquiring and tracking the signal. However, it was noted that significant distortions were present even when the PSF was centered over the sensor, likely the result of mechanical stress on the panel introduced by the mounting structure. In addition the panel was found to be tilted in elevation, which likely caused cross-coupling in the estimates. These mechanical problems will have to be resolved by removing the tilt and reducing the stress on the panel, in order to reduce distortions in the PSF and cross-coupling in pointing, before collecting more optical data. After these modifications have been completed, plans are to continue tracking weaker optical sources such as stars first at night, then into the early morning hours to determine the impact of background light on the detectability of optical sources.

V. REFERENCES

[1] V. Vilnrotter, D. Hoppe, B. Moision, J. Charles, “Optical Communications Performance of Hybrid 34-meter Microwave Antennas,” IEEE Aerospace Conference, Big Sky, MN, March 2010.

[2] V. Vilnrotter, M. Srinivasan, “Adaptive Detector Arrays for Optical Communications Receivers,” IEEE Transactions on Communications, Vol. 50, Issue 7, 2002, pp. 1091-1097.

[3] V. Vilnrotter, C.-W. Lau, M. Srinivasan, K. Andrews, R. Mukai, “Optical Array Receiver for Communication through Atmospheric Turbulence,” Journal of Lightwave Technology, Vol. 23, Issue 4, 2005, pp. 1664-1675.

Acknowledgments: The author would like to acknowledge the contributions of team members Daniel Hoppe, Theodore Hanson, Asim Sehic, and Philip Tsao for fabricating and installing the polished panels, camera enclosure and computer interface on the DSS-13 antenna, and helping with the characterization of the Vertex panel on the JPL mesa test range.

The research described in this paper was carried out at the Jet Propulsion Laboratory, California Institute of Technology, under a contract with the National Aeronautics and Space Administration.